J Therm Spray Tech (2020) 29:1172–1182
https://doi.org/10.1007/s11666-020-01022-9

PEER REVIEWED

Fabrication of TiO_2-$SrCO_3$ Composite Coatings by Suspension Plasma Spraying: Microstructure and Enhanced Visible Light Photocatalytic Performances

Mengjiao Zhai[1,2,3] · Yi Liu[2,3] · Jing Huang[2,3] · Wenjia Hou[2,3] · Songze Wu[2,3] · Botao Zhang[2,3] · Hua Li[2,3]

Submitted: 28 July 2019 / in revised form: 3 February 2020 / Published online: 18 March 2020

Abstract A novel TiO_2-$SrCO_3$ co-catalyst with a porous structure was fabricated by suspension plasma spraying. $SrTiO_3$ as revealed by high-resolution TEM was formed by the chemical reaction of TiO_2 with $SrCO_3$ during the high-temperature plasma spraying. A narrow band gap (2.58 eV) and reduction in the recombination speed of photoinduced carriers of the coatings were detected by UV–visible diffuse reflectance spectrometry and fluorescence spectrometry, respectively. The enhanced visible light-driven photodegradation properties of the coatings resulted in promoted degradation of methylene blue. The composite coatings also demonstrated significantly pronounced bactericidal activities against the Gram-negative bacterium *Escherichia coli* than the pure TiO_2 coatings, achieving a killing rate of over 99.7%. The results give insights on the potential to fabricate large-scale nano-TiO_2-based porous photocatalytic coatings by suspension plasma spraying for versatile environmental applications.

✉ Yi Liu
liuyi@nimte.ac.cn

✉ Hua Li
lihua@nimte.ac.cn

[1] Faculty of Materials Science and Chemical Engineering, Ningbo University, Ningbo 315211, Zhejiang, China

[2] Key Laboratory of Marine Materials and Related Technologies, Ningbo Institute of Materials Technology and Engineering, Chinese Academy of Sciences, Ningbo 315201, China

[3] Cixi Institute of Biomedical Engineering, Ningbo Institute of Materials Technology and Engineering, Chinese Academy of Sciences, Ningbo 315201, China

Graphic Abstract

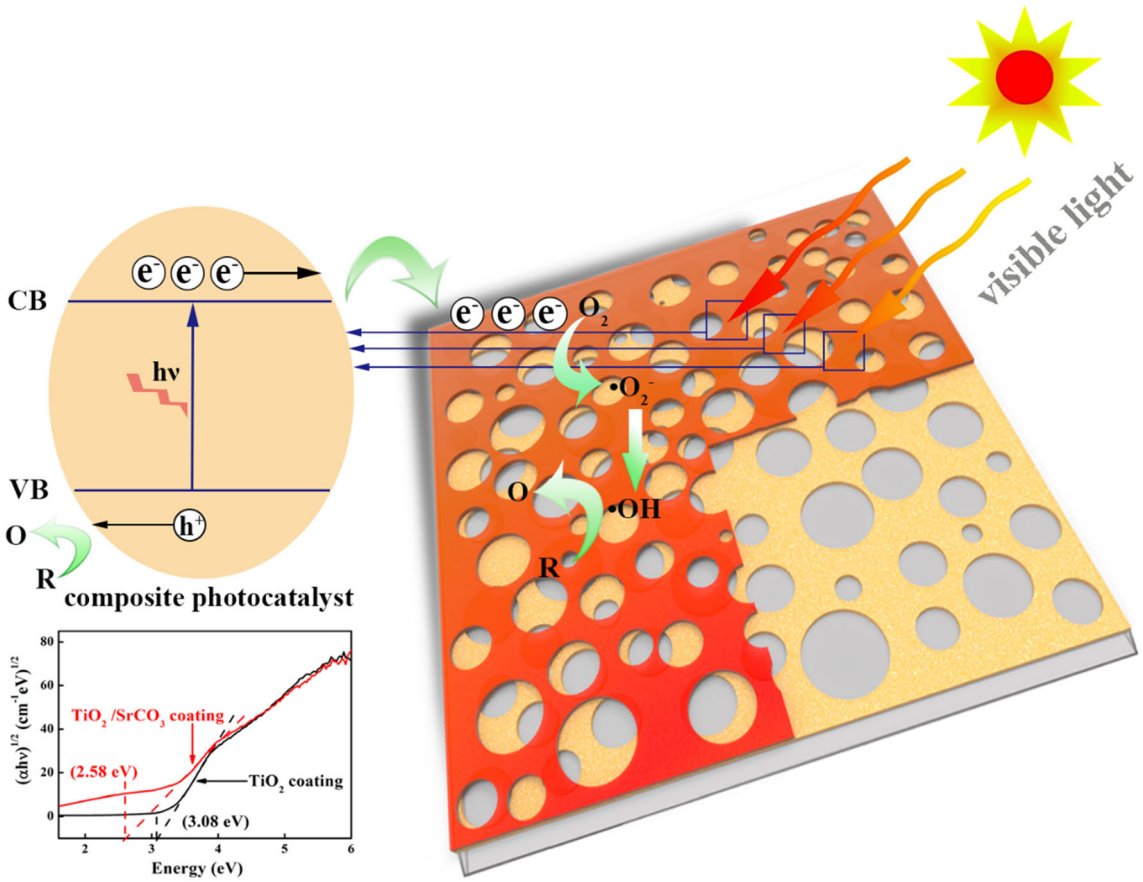

Keywords antibacterial performances · porous photocatalytic coatings · suspension spraying · TiO_2-$SrCO_3$ coatings · visible-light absorption

Introduction

Advanced oxidation processes (AOPs) have gained great popularity during the last decade owing to their versatile environmental applications, including organic pollutant degradation (Ref 1, 2), wastewater purification (Ref 3, 4), deodorization (Ref 5), decontamination and sterilization (Ref 6). The action mechanisms of AOPs are based on the generation of reactive species (i.e., H_2O_2, OH, O^{2-}, O_3) via O_3/UV reactions, O_3/H_2O_2 processes, UV/TiO_2 catalysis and Fenton or UV/Fenton reactions (Ref 7, 8). Among all AOPs, in terms of environment protecting and energy saving, the photocatalysis process by means of utilizing advanced catalysts has its inherent advantages. Photocatalysis aims to initiate or accelerate reduction and oxidation (redox) reactions by the light–matter interaction (Ref 9, 10). Various catalysts (TiO_2, ZnO, Fe_2O_3, CdS, GaP and ZnS) have been intensively explored in newly developed energy storage (Ref 11) and environmental purification (Ref 12) systems.

Among the photocatalysts, TiO_2 has attracted intense attention due to its non-toxicity, cost-efficiency, thermal and chemical stability and environment friendliness (Ref 4, 13). In principle, due to its wide band gap (3-3.2 eV), TiO_2 can absorb light within the ultraviolet range and hinder the photogenerated electron–hole recombination. However, this kind of light (360-380 nm) accounts for no more than 5% of the total solar energy reaching the surface of the earth (Ref 14). For better utilization of sunlight, there have been persistent efforts to enhance the photocatalytic property of TiO_2 through a variety of techniques like modifying its structure with noble metal loading, metal ion doping, anion doping, dye sensitization, metal ion implantation and coupling with other semiconductors (Ref 5). Among these techniques, the development of the semiconductor–semiconductor structure has been proven beneficial to photocatalysis in four ways: (1) widening the light absorption range to the visible region, (2) enhancing the photogenerated carrier separation (Ref 15), (3) alleviating the photogenerated charge carrier recombination (Ref 16) and (4) protecting the narrow bandgap catalyst from photocorrosion (Ref 17, 18). An example is the coupling

effect between CdS and TiO_2, which demonstrated enhanced charge separation under visible light illumination (Ref 19). Besides, the combination of n-type $SrTiO_3$ (Eg = 3.3 eV) and n-type TiO_2 (Eg = 3.2 eV) is a representative example of coupling two materials that have band gaps close to each other (Ref 20, 21). During this process, the light absorption range of the semiconductor is not affected. The band offset was reported to accelerate the charge separation and inhibit the photogenerated charge recombination (Ref 18). It was noted that, as a semiconductor with a band gap similar to TiO_2 and easy acquisition, $SrCO_3$ was traditionally used as an additive in glass cathode ray tubes and a constituent of magnetic ferrite in DC motors (Ref 22). It has also been used in the production of fireworks, rainbow glass and PTC thermistor components (switch start, degaussing, current limiting protection, constant temperature heating, etc.) (Ref 23). Nevertheless, there are few reports available so far pertaining to the photocatalysis performances of $SrCO_3$ (Ref 24, 25).

Coating processes like sol–gel method, hydrothermal method, chemical vapor deposition, physical vapor deposition and electrodeposition have been adopted to synthesize the semiconductor–semiconductor structure (Ref 18). However, application of these approaches is limited due to either long preparation periods or strict experimental conditions. Recently, plasma spraying has been proposed as a versatile coating technique due to its cost-efficiency, convenient operation and merits in fabrication of controllable nanostructure (Ref 26, 27). In this study, suspension plasma spraying was utilized for the first time to fabricate the semiconductor–semiconductor nanostructures with remarkably enhanced UV and visible light adsorption properties. Desired topographies of the deposited TiO_2-$SrCO_3$ coatings were produced by modification of spraying parameters. The microstructure, phase composition and photocatalytic performances were investigated and discussed.

Materials and Methods

Coatings were fabricated by suspension plasma spraying (APS-2000K system, Beijing Aeronautical Manufacturing Technology Research Institute, China). The suspension used for plasma spraying was prepared by blending 20 g $SrCO_3$ (Sinopharm Chemical Reagent Co., Ltd $\geq$ 99.0%,) with 20 g Degussa TiO_2 (Evonik Degussa P25, 99.5%) in 400 ml 50% ethanol solution containing 8 g polyvinylpyrrolidone (PVP) and 2 g polyethylene glycol (PEG) under continuous mechanical stirring. The feedstock feeding system was established using a peristaltic pump with a flow rate of 60 ml/min to a ϕ0.7 mm spray-atomized injector. Compressed air with pressure of 0.6 Mpa was used for suspension atomization. During the spraying process, argon at a flow rate of 15 ml/min and under a working pressure of 0.75 MPa was used as the primary plasma gas. In the meantime, hydrogen at a flow rate of 1.8 ml/min and under a working pressure of 0.3 MPa was used as the secondary plasma gas. The plasma power ranged from 27 to 33 kW. All the coatings in this work were fabricated with the gun moving parallel to the substrate with two spray passes at a speed of 400 m/min and a spraying distance of 80 mm. For comparison purposes, pure TiO_2 suspension was prepared by dispersing 40 g Degussa TiO_2 in the identical base liquid medium and coatings were fabricated following the same protocol. All coatings were deposited on sand-blasted 316L stainless steel plates and left to cool for 10 min after spraying. Grit blasting was carried out using corundum-based particles of 50-150 μm with compressed air of 5 bar. For all substrates, it was propelled with an impact angle of about 45° and target distance of around 100 mm.

The morphologies of the coatings were characterized by field emission scanning electron microscopy (FESEM, FEI Quanta FEG250, the Netherlands). The chemical composition of the samples and the phase composition of TiO_2 were characterized by x-ray diffraction (XRD, Bruker AXS, Germany) at a scanning rate of 0.1°/s using Cu Ka radiation operated at 40 kV. Further characterization of surface chemistry was achieved using Fourier transform infrared spectroscopy (FTIR, model 6300, BioRad Co. Ltd., USA) with a resolution of 8 cm^{-1} and a scan number of 4 at a spectral region ranging from 400 to 3600 cm^{-1}. The light absorption spectra of the coatings were acquired using UV–visible diffuse reflectance spectrometry (UV–vis DRS) with $BaSO_4$ as the reference. Fluorescence spectrometry (FL3-111, Horiba, France) was used to acquire the fluorescence spectra. High-resolution transmission electron microscopy (HRTEM, FEI Tecnai F20, the Netherlands) was employed to explore the detailed microstructure of the coatings. For TEM characterization, the coatings were scraped from the substrates and supersonically dispersed in ethanol. The suspensions were transferred onto copper micro-grids and dried under infrared light.

Photocatalytic activities of the coatings (20 × 20 mm^2) were assessed by examining the photodegradation of methylene blue (MB, Aladdin Reagent Corporation, China). For the degradation testing, each piece of the samples was immersed in MB solution (15 ml, 5 ppm) and positioned 15 cm below the lamp (UV light, Philips, TL-D, 15 W and Xe lamp, GXZ500) in a double-walled beaker which can avoid thermal effect with the help of cooling circulating water. After being placed in the dark for 1 h with magnetic stirring to ensure adsorption/desorption equilibrium, the degradation of MB under light was examined by detecting the absorption at 664 nm using a

UV–vis spectrophotometer (MAPADA, UV-3300 spectrophotometer) every hour. For assessment of the bactericidal properties of the coatings, Gram-negative bacterium *Escherichia coli* ATCC25922 was used as the target bacteria. The Luria broth (LB) medium was prepared following an established protocol reported previously (Ref 28) and used to incubate *E. coli* in a shaker operated at 120 rpm for 24 h at 30 °C. The media containing the bacteria were centrifuged at 2000 rpm for 5 min to remove the supernatant, and the cell pellets were washed three times with 0.85% NaCl solution. A bacterial suspension with a concentration of 5×10^7 CFU/mL was obtained by resuspending the cleaned cell pellet in 0.85% NaCl solution, and 4 mL suspension was added into each well of sterilized 6-well plates. Samples were subjected to UV light (200-280 nm) treatment for 5 h to avoid contamination before antibacterial tests. To carry out the antimicrobial test and avoid interference from other factors, 6-well plates containing the bacterial suspension and samples were placed 15 cm below a UV lamp (Philips, TL-D, 15 W) in an oscillating microorganism incubator. After being cultivated at 120 rpm for 24 h at 30 °C, 2 μL bacterial suspension from each well after UV illumination was diluted and plated on nutrient agar plates. The number of bacteria was counted after incubating the plates at 37 °C for 16 h. The colony-forming units (CFUs) of the bacteria were examined, and the killing rate is calculated according to Eq. (1), where the control group represented pure bacterial suspension without the coating samples.

$$\text{Bactericidal rate } (\%) = \frac{\text{CFUs of control group} - \text{CFUs of experimental group}}{\text{CFUs of control group}} \times 100\% \quad \text{(Eq 1)}$$

Results and Discussion

During spraying, the suspension feedstock was transferred into a high-temperature ionized gas that was created with the mixed gas passing through a struck DC arc. After being heated and accelerated by the ionized gas, the injected drops were fragmented, vaporized and cooled to form the coatings on the substrate surfaces. The morphologies of the coatings are therefore closely related to spraying parameters and physical–chemical properties of the initial feedstock. Figure 1 shows the SEM images of TiO_2-$SrCO_3$ composite coatings deposited by suspension plasma spraying with the plasma power of 27, 30 and 33 kW. The low spraying power resulted in an irregular surface structure of the coatings that consisted of clustered particles (Fig. 1a-1). The spherical particles are clearly seen on the top layer of the coatings (the red circles in Fig. 1a-2), which were likely attributed to the gas produced by sudden decomposition of PVP at high temperature and failed to escape from the surrounding particles. The sphere was left after the droplets impacted on the cold substrate (Ref 29).

The stacked particles would give rise to insufficient mechanical strength of the coating and its bonding with the substrate. We therefore developed a novel layered porous coating structure, and each porous layer was fabricated with the plasma power level of 30 kW. As the liquid feedstock encountered the plasma jet with a higher power, the fast evaporation and decomposition of the pyrolyzed materials made them apt to escape from the molten particles, leaving pores in the coating when deposited on a cold substrate. This phenomenon has been elucidated in a previous study (Ref 29). Interlamellar pores (Fig. 1b-2) offered a large specific surface area and possibly facilitated mass transfer. Besides, apart from releasing gas due to decomposition, the residual PVP also served as a bonding agent to ensure the bonding among semi-molten particles. Further augmented spraying power resulted in increased temperature and velocity of the plasma jet accordingly. As a result, the gas and steam pressure exerted on surrounding particles increased, resulting in the partially disappearance of the layered structure and the porous structure, as shown in Fig. 1c. Therefore, in this case, the plasma power of 30 kW was chosen for subsequent coating deposition. The thickness of the coating was approximately 55 μm (Fig. 1e). It was noted that the coating deposited using pure TiO_2 feedstock also presented a porous morphology (Fig. 1d), but did not form a regular layered porous structure. This nevertheless suggests the contribution of the $SrCO_3$ decomposition to constructing porous frameworks during spraying process:

$$SrCO_3\,(s) \overset{900-1150\,^{\circ}C}{\rightarrow} SrO\,(s) + CO_2\,(g).$$

During spraying, SrO was easily produced and the generated CO_2 was simultaneously released (Ref 30). The merit of the decomposition reaction of $SrCO_3$ or PVP is mainly the release of gas which increased the porosity of the coating. The occurrence of these reactions was verified by XRD and FTIR analyses (Fig. 2).

The strong and broad band located at 3420 cm^{-1} of the IR peaks are attributed to the water absorbed on PVP

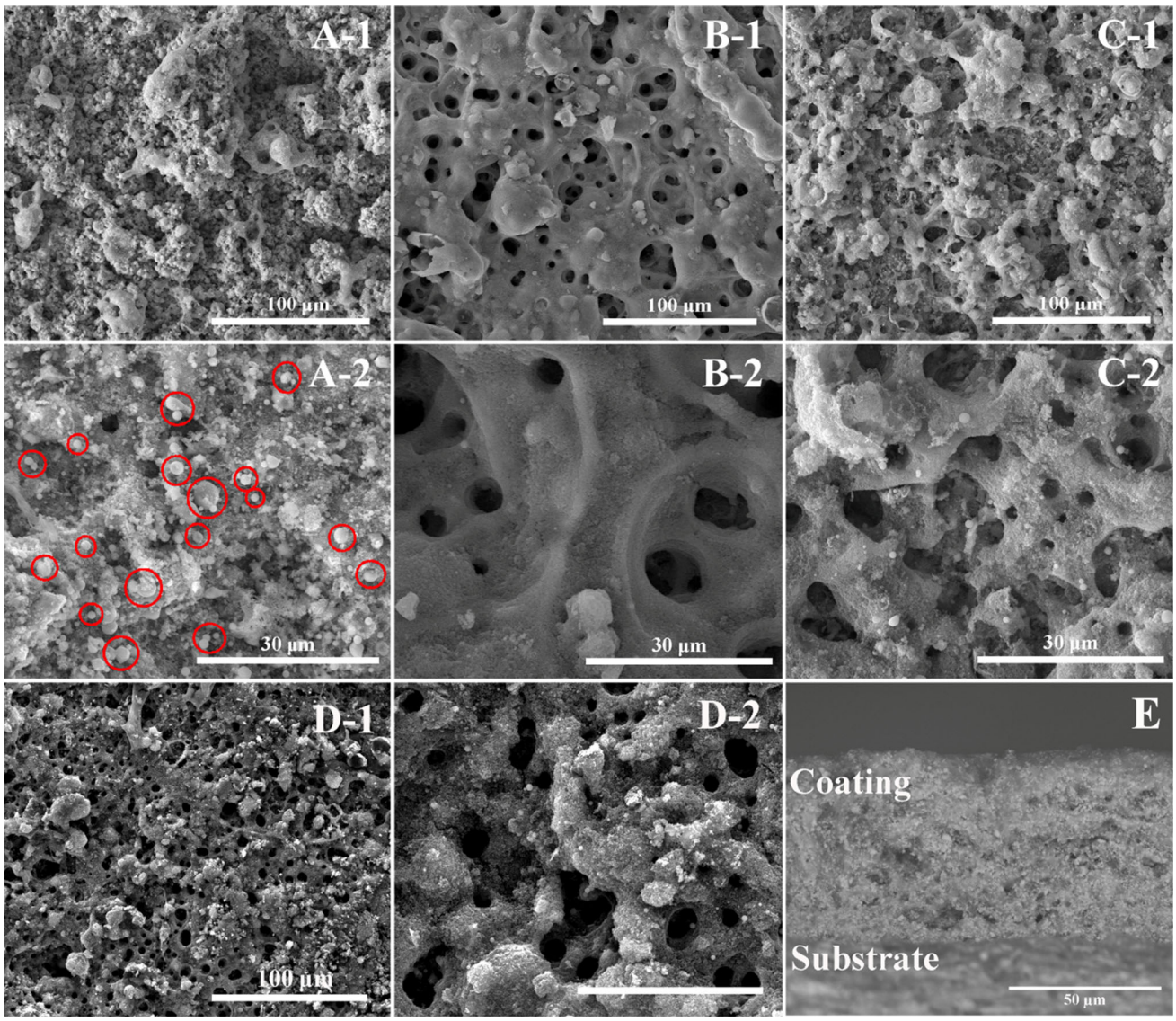

Fig. 1 SEM images of the TiO_2-$SrCO_3$ coatings fabricated under the plasma powder of 25 kW (a), 30 kW (b) and 33 kW (c), and the pure TiO_2 coating was deposited under 30 kW (d); and e: typical cross-sectional morphology of the TiO_2-$SrCO_3$-$SrTiO_3$ coating. (− 2 is enlarged view of selected area shown in − 1)

surfaces, hydrogen-bonded OH groups (Ref 31) and the stretching vibration of carbonyl on pyrrolyl (Ref 32). The peaks located at 2924-2843, 1671, 1462 and 1286 cm^{-1} are attributed to the C–H stretching, C=O stretching vibration, $–CH_2–$ stretching and C–N stretching vibration of PVP molecules, respectively (Ref 33, 34). FTIR spectra of the pure TiO_2 coating and the TiO_2-$SrCO_3$ coating both show the peaks relating to PVP at 2889, 1671, 1462 and 1286 cm^{-1}, indicating the residual PVP in the coatings. Since the FTIR spectra were obtained after background removal, the signal at 2500 cm^{-1} is ascribed to CO_2 that was generated from the decomposition reaction of $SrCO_3$ and absorbed to the coating surface as adsorbate (Ref 35, 36). These results suggest that the PVP in the suspension was partly decomposed during the spraying process, and the remaining PVP served as the bonding agent among the unmelted and semi-molten particles to ensure the integrity of the coating. The broad band located at 700-1000 cm^{-1} of the pure TiO_2 coating refers to Ti-O and Ti-O-Ti skeletal frequency region (Ref 37). However, there are weak bands located at 625 and 790 cm^{-1} for the composite coating, corresponding to TiO_6 stretching and octahedron bending, respectively (Ref 38). This means the formation of the perovskite structure. In addition, the peaks at 1430 cm^{-1} and 1770 cm^{-1} are associated with the symmetric stretching and the C=O stretching vibrations of CO_3^{2-}. The peaks observed at 1422, 862 and 708 cm^{-1} are attributed to the C-O asymmetric stretching, out-of-plane bending and in-plane bending of CO_3^{2-}, respectively. The infrared spectrum presents a weak band at 448 cm^{-1},

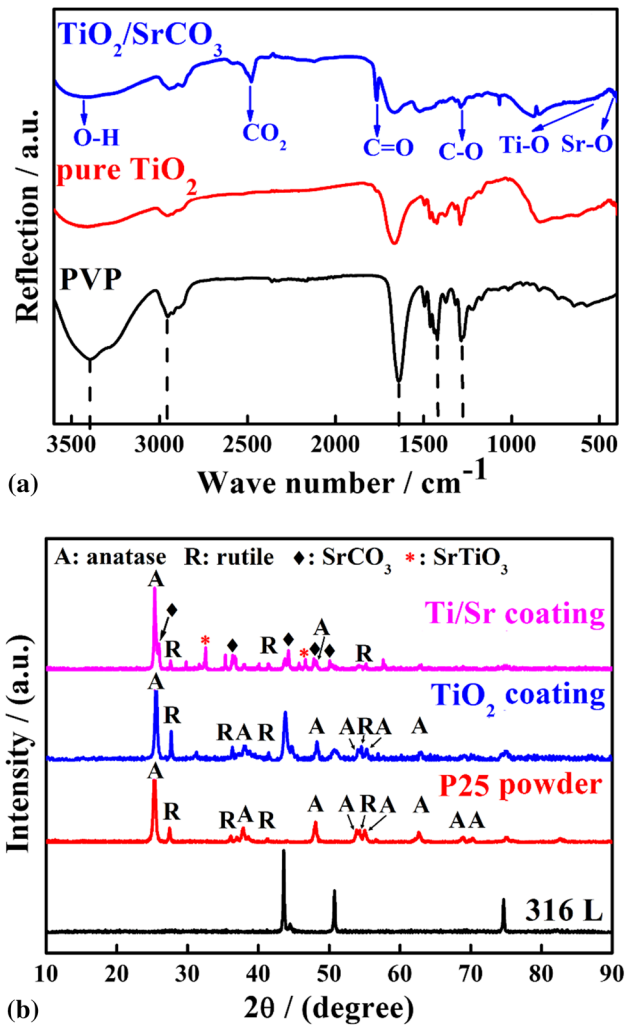

Fig. 2 FTIR spectra (a) and XRD curves (b) of the pure TiO_2 coating and the TiO_2-$SrCO_3$ coating

associated with the SrO stretching, confirming the presence of Sr-based compounds in the coatings (Ref 39). The FTIR spectra of the composite corroborates that the deposited coating are composed of TiO_2, $SrCO_3$ and $SrTiO_3$ compounds because the peaks are complete correspondence. According to the decomposition reaction of $SrCO_3$ discussed previously, the decomposition occurs at around 1000 °C, which is much lower than the temperature of the plasma jet (usually up to 10,000 °C) (Ref 40). However, XRD detection did not show the trace of SrO in the samples, which is very likely due to a small amount of SrO.

The XRD diffractogram (Fig. 2b) shows the strong peak at 25.3° which is attributed to the (001) plane of anatase, and the weak peaks at 27.5° and 54.3° which correspond to the (110) and (211) plane of rutile. Both the pure TiO_2 coating and the composite coating exhibited similar phase composition to pristine P25, indicating the anatase of TiO_2 was well-retained after high-temperature process. The peaks at 25.4°, 45.8°, 47.8° and 50.3° are assigned to undecomposed $SrCO_3$. Furthermore, the formation of $SrTiO_3$ in the coatings was further detected by TEM. These phases would ultimately influence the photocatalytic performances of the coatings.

TEM analyses were conducted to further characterize the TiO_2-$SrCO_3$ composite structure and evidence the presence of $SrTiO_3$ in the inner structure (Fig. 3). The phase transformation from anatase to rutile was reported to occur with the growth of grain size (Ref 41). Some crystals as well as discrete particles had an approximate particle size of 5-50 nm (Fig. 3a), and most particles had a diameter of around 25 nm, which is consistent with the size of the pristine P25 particles and in agreement with the XRD results. The high-resolution transmission fringes of the selected area I and corresponding selected area electron diffraction (SAED) pattern shown in Fig. 3b and c suggest a polycrystalline structure, which can be indexed as the (101), (112), (004) plane of anatase, the (021), (002) crystal plane of rutile, and the (110), (223), (310) plane of strontium carbonate. Growth of $SrTiO_3$ on TiO_2 lattice was confirmed by the faint fringe attributed to the (211) plane from the HRTEM image of the composite coating. Interestingly, the coexistence of $SrCO_3$ and $SrTiO_3$ was observed, which could improve the catalytic activity and inhibit deactivation of the catalysts, since $SrCO_3$ can extract photoinduced electrons from conduction band of $SrTiO_3$ to accelerate the separation of photoinduced charge carriers (Ref 25). However, the presence of strontium oxide was not clearly detected by TEM, presumably due to the easy reaction of strontium oxide with H_2O and CO_2 in air (Ref 42). A large number of irregular spots on the diffraction pattern as shown in Fig. 3d indicate the presence of doping and disordered structures in the crystal lattice. The existence of moiré pattern was marked by the dotted box and the dislocations and small-angle grain boundaries were highlighted by the arrows (Fig. 3c). The small misorientation on the interface can lead to imperfect oriented attachment and generate localized dislocations (Ref 43). The influence of the formation of secondary phases and small-angle boundaries, disorders and crystal defects on semiconducting properties may be substantial by providing a guiding center to optical excitation and relaxation and hindering the recombination speed of light-induced electrons and holes (Ref 44, 45). It is worth noting that the composite particles subjected to plasma spraying presented a thin amorphous surface layer with a thickness of 1 nm or less (Fig. 3b). It has been proven that the generation of a disordered layer can lead to the narrowing of the optical band gap (Ref 44). Hence, it is anticipated that the composite structure would have a narrower band gap than the pristine catalysts. Taken together, the TiO_2-

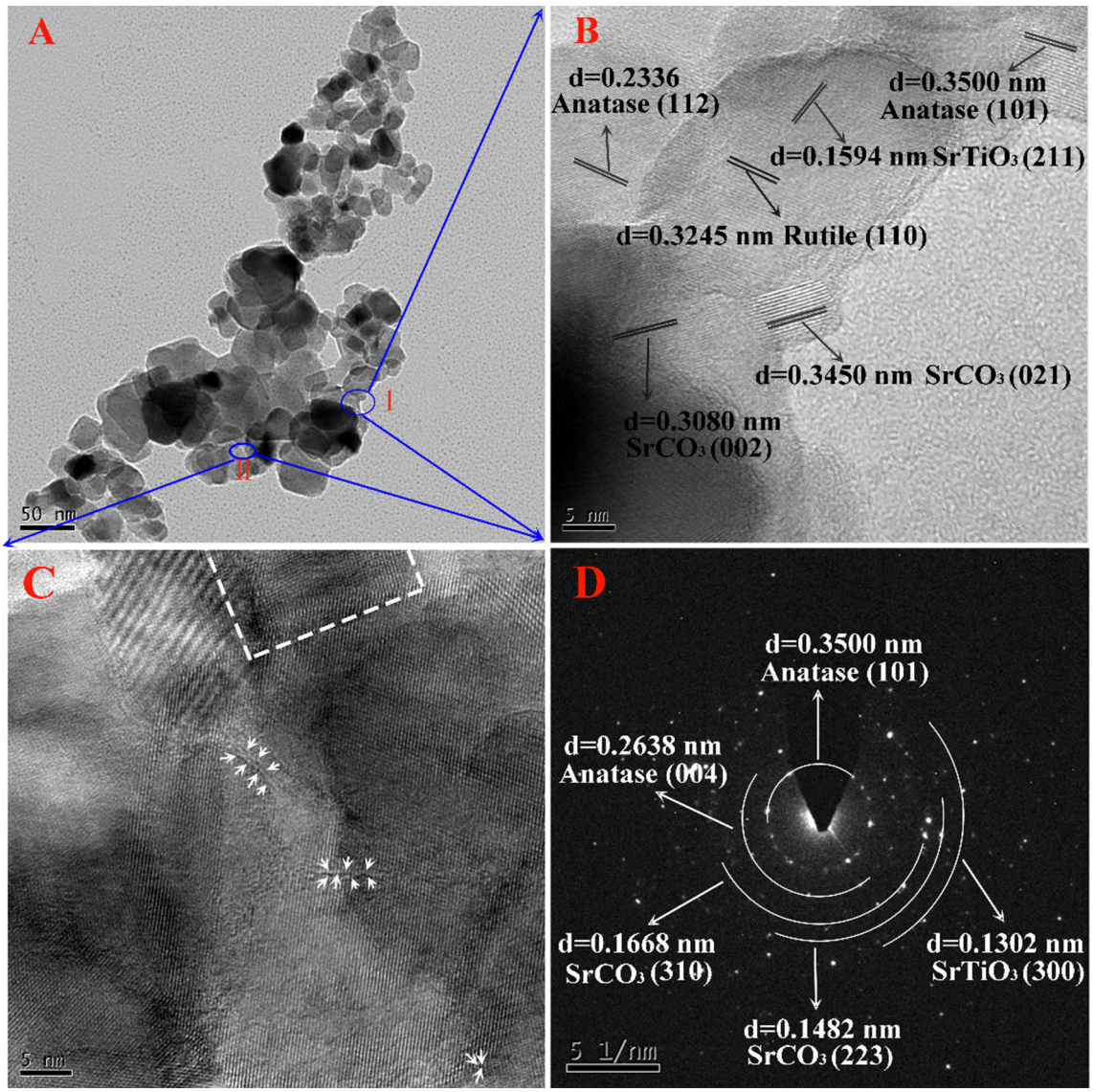

Fig. 3 TEM imaging analyses of the coatings fabricated under the plasma powder of 30 kW, a: TEM image of the TiO_2-$SrCO_3$ coating; b, c: HRTEM images of the selected area I and II; d: SAD pattern of the composite coating

$SrCO_3$ composite photocatalyst with secondary phases and disordered microstructure are expected to enhance the photocatalytic performance, as shown in the following.

Light absorption and photoexcitation mainly depend on the band gap (Eg) of semiconductors. In this study, UV–vis diffuse reflectance spectrometry (DRS) was employed to examine the band gap energy and light absorption ability of the coatings in the wavelength range of 200-800 nm. It was observed that both coatings exhibited significant absorption within the UV region between 200 and 350 nm (Fig. 4a). Furthermore, a notable absorption extension comparable to that in the UV light region was observed in the visible light region for the composite coating, while no obvious absorption peak was detected in the visible spectrum for the pure TiO_2 coating. These results closely agreed with the TEM results and validated a greatly enhanced optical absorption intensity of the composite coating. Compared with the TiO_2 coating, the absorption edge of the composite coating slightly shifted to longer wavelengths, indicating that the doping in the composite coating influenced the main structure of the catalyst (Ref 46). With the anatase as the main phase, the band gap value of TiO_2 was estimated by the Tauc plot as an indirect semiconductor according to a previous report (Ref 47). As shown in Fig. 4b, the band gap of the pure TiO_2 coating was 3.08 eV, being consistent with that of pristine P25. The composite coating had a narrower band gap of 2.58 eV; thus, the presence of $SrCO_3$-$SrTiO_3$ reduces the band gap value (Table 1), which is beneficial to the formation of photoinduced electron–hole pairs because less excitation energy is needed in this

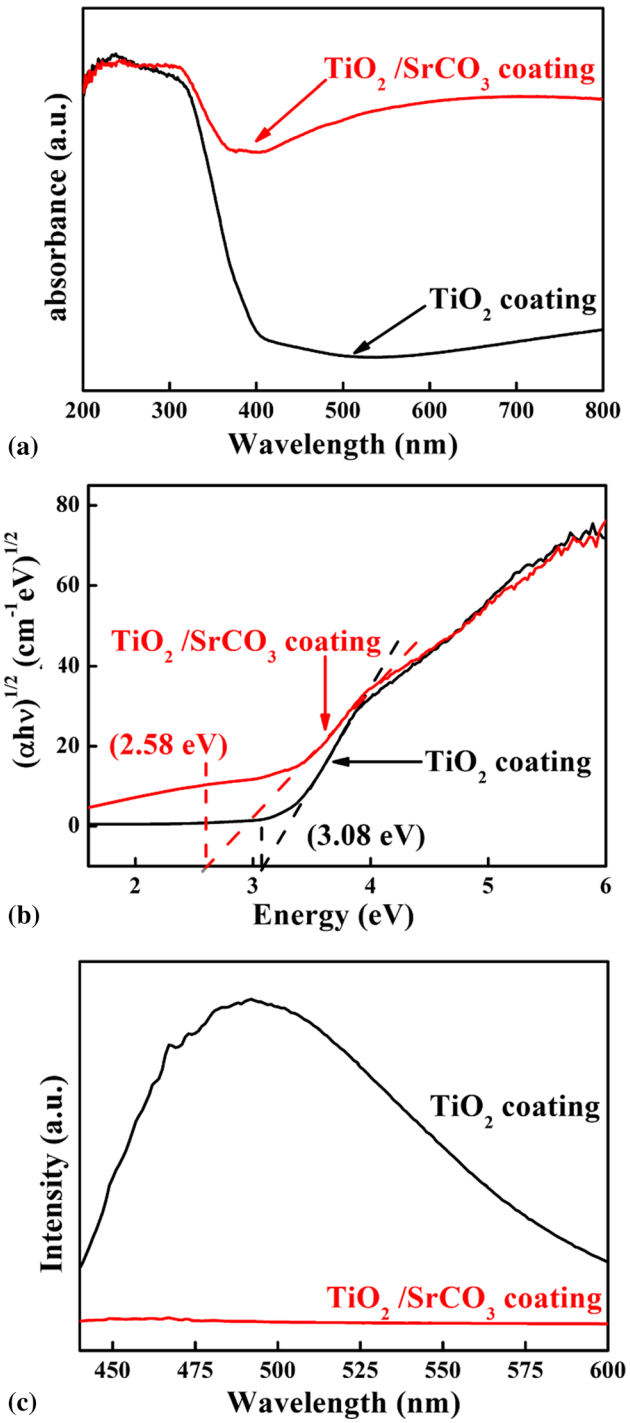

Fig. 4 Spectral absorbance (a), Tauc plot (b), and PL spectra (c) of the TiO_2-$SrCO_3$ coatings fabricated under the plasma powder of 30 kW

case. However, fast separation is another critical issue during photocatalysis. In this case, photoluminescence (PL) emission spectroscopy was carried out to investigate the separation of electron hole pairs. The emission peak was derived from the recombination of electrons and holes and an enhanced charge carrier separation should give rise to a low-intensity emission peak (Ref 48). As shown in Fig. 4c, the pure TiO_2 coating had a strong PL peak at $\sim$ 490 nm. Whereas the PL intensity of the composite coating is significantly weaker, proving the capability of the TiO_2-$SrCO_3$ composite coating to enhance the separation of the photogenerated charge carriers and produce more surface carriers. The composite coating is therefore able to provide further promoted photocatalytic performances.

Table 1 The band gap energy (Eg) of phases

Materials	TiO_2	$SrCO_3$	$SrTiO_3$
Eg, eV	3.08	5.14	3.24

The role of addition of $SrCO_3$ on photocatalytic performance of the porous coatings was examined by degrading MB dye in aqueous solution under the irradiation of UV and visible light (Fig. 5). After 1 h of adsorption/desorption equilibrium, a negligible photodegradation of MB was detected in the absence of photocatalysts. When the pure TiO_2 coating and the composite coating were exposed to UV light, 63.9% and 83.4% of MB were decomposed after 6 h, respectively, suggesting that the composite coating was more effective. When placed under visible light, the composite coating showed increased photocatalytic activities (87.8%) while the TiO_2 coating demonstrated decreased photocatalytic activities (56.2%). The Langmuir–Hinshelwood first-order kinetic model $\ln(\frac{C_0}{C}) = k_{app} \times t$ was then used to further elucidate the photocatalytic properties of the samples, where k is the apparent rate constant, C_0 is the initial concentration of the MB solution after the adsorption–desorption equilibrium process and C refers to the residual concentration of the solution at regular time intervals under UV light or visible light irradiation. The k values of different samples under different light resources are shown in Fig. 5c and d. The k values for MB degradation by the composite coating under UV light (0.2606 h^{-1}) and visible light (0.29135 h^{-1}) illumination are about 2 and 3 times higher than those for the pure TiO_2 coating (0.13564 and 0.10693 h^{-1}, respectively). The higher efficiency of the composite coating (especially under visible light irradiation) could be attributed to the coupling of TiO_2 and $SrCO_3$, the generation of $SrTiO_3$ and the presence of the disordered structure (Ref 20, 21, 44). Those structural features presumably resulted in the reduction of energy gap and provided additional electronic states among conduction and valence bands.

The bactericidal effect of the coatings was further examined (Fig. 6). As expected, a maximum number of colonies was found for the blank group. All samples showed reduced growth of bacterial colonies after UV light

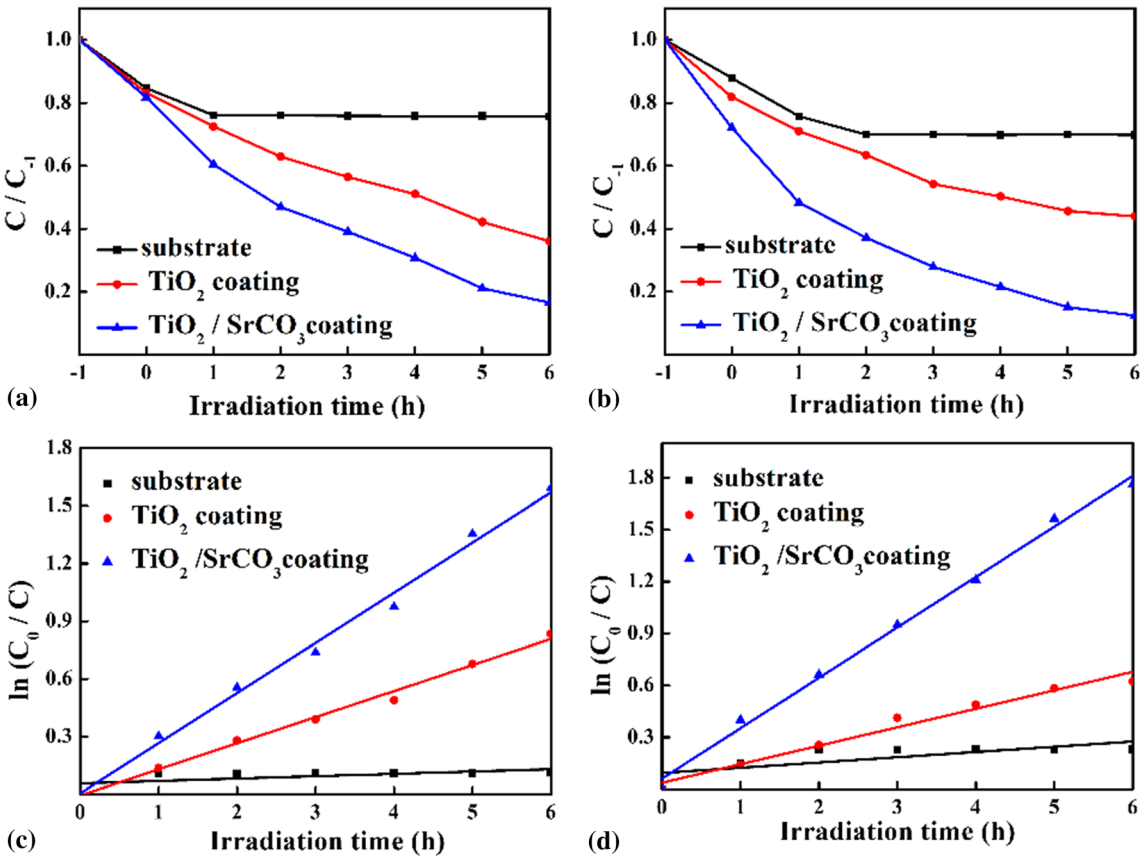

Fig. 5 Photocatalytic degradation of MB of the pure TiO_2 coating and the TiO_2-$SrCO_3$ coating under UV light (a) and Xe lamp (b) irradiation and linearly transformed ln (C_0/C) of the kinetic curves of MB degradation under the UV light (c) and Xe lamp (d) irradiation

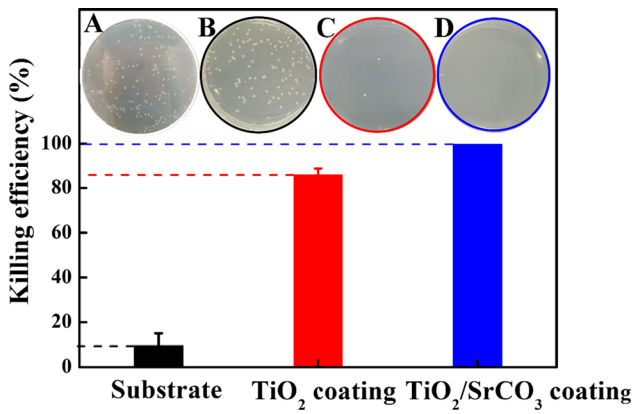

Fig. 6 The inactivation efficiency of *E. coli* by different samples. a Blank; b substrate; c TiO_2 coating fabricated under the plasma powder of 30 kW; d TiO_2-$SrCO_3$ coating fabricated under the plasma powder of 30 kW

illumination, and the antibacterial activity of the composite coating was significantly more pronounced than that of the other samples. The killing rate of the substrate and the TiO_2 coating was 9.7% and 86.1%, respectively, while that of the composite coating was over 99.7%. Living organisms consist of abundant organic compounds which can be easily damaged by the reactive oxygen species (ROS) generated by photocatalytic reactions. In detail, bacterial death is believed to be a consequence of a significant disorder in cell permeability and the decomposition of the cell wall (Ref 49). This result clearly indicates the excellent bactericidal ability of the composite coating.

Conclusions

In summary, suspension plasma spraying showed appropriateness in fabricating the novel TiO_2-$SrCO_3$ composite photocatalyst. The composite coatings showed a unique layered porous microstructure and a well-reserved nanostructure. The special structure and the co-catalyst effect offered by $SrTiO_3$ resulted in accelerated generation and inhibited recombination of photogenerated electrons and holes. Significantly enhanced photodegradation effects of MB dye under both UV and visible light, along with outstanding antibacterial performances, were revealed for the TiO_2-$SrCO_3$ coating. These results shed light on developing nano-titania-based photocatalytic surface coatings for

potential applications in environmental remediation and antibiosis.

Acknowledgments This work was supported by Key Research and Development Program of Zhejiang Province (Grant # 2017C01003), National Science Foundation of China (Grant # 31500772), Zhejiang Provincial Natural Science Foundation of China (Grant # LY18C100003) and International Scientific and Technological Cooperation Project of Ningbo (Grant # 2017D10011).

References

1. C.C. Wang, J.R. Li, X.L. Lv, Y.Q. Zhang, and G. Guo, Photocatalytic Organic Pollutants Degradation in Metal-Organic Frameworks, *Energy Environ. Sci.*, 2014, **7**, p 2831–2867
2. J.J. Pignatello, E. Oliveros, and A. MacKay, Advanced Oxidation Processes for Organic Contaminant Destruction Based on the Fenton Reaction and Related Chemistry, *Crit. Rev. Environ. Sci. Technol.*, 2006, **36**(1), p 1–84
3. J.-L. Wang and L.-J. Xu, Advanced Oxidation Processes for Wastewater Treatment: Formation of Hydroxyl Radical and Application, *Crit. Rev. Environ. Sci. Technol.*, 2012, **42**(3), p 251–325
4. M. Horáková, Š. Klementová, P. Kříž, S.K. Balakrishna, P. Špatenka, O. Golovko, P. Hájková, and P. Exnar, The Synergistic Effect of Advanced Oxidation Processes to Eliminate Resistant Chemical Compounds, *Surf. Coat. Technol.*, 2014, **241**, p 154–158
5. M. Pelaez, N.T. Nolan, S.C. Pillai, M.K. Seery, P. Falaras, and A.G. Kontos, A Review on the Visible Light Active Titanium Dioxide Photocatalysts for Environmental Applications, *Appl. Catal. B Environ.*, 2012, **125**, p 331–349
6. W. Pawlak, M. Jakubowska, A. Sobczyk-Guzenda, M. Makówka, H. Szymanowski, B. Wendler, and M. Gazicki-Lipman, Photo Activated Performance of Titanium Oxide Coatings Deposited by Reactive Gas Impulse Magnetron Sputtering, *Surf. Coat. Technol.*, 2018, **349**(15), p 647–654
7. P. Saritha, D.S.S. Raj, C. Aparna, P.N.V. Laxmi, V. Himabindu, and Y. Anjaneyulu, Degradative Oxidation of 2,4,6 Trichlorophenol Using Advanced Oxidation Processes—A Comparative Study, *Water Air Soil Pollut.*, 2009, **200**(1–4), p 169–179
8. J.M. Britto and M.C. Rangel, Advanced Oxidation Process of Phenolic Compounds in Industrial Wasterwater, *Quim. Nova.*, 2008, **31**, p 114–122
9. F. Wang, Q. Li, and D. Xu, Recent Progress in Semiconductor-Based Nanocomposite Photocatalysts for Solar-to-Chemical Energy Conversion, *Adv. Energy Mater.*, 2017, **7**(23), p 1700529
10. H. Tong, S. Ouyang, Y. Bi, N. Umezawa, M. Oshikiri, and J. Ye, Nano-Photocatalytic Materials: Possibilities and Challenges, *Adv. Mater.*, 2012, **24**(2), p 229–251
11. X.-Z. Liu, K. Wen, C.-M. Deng, K. Yang, C.-G. Deng, M. Liu, and K.-S. Zhou, Nanostructured Photocatalytic TiO_2 Coating Deposited by Suspension Plasma Spraying with Different Injection Positions, *J. Therm. Spray Technol.*, 2018, **27**(3), p 245–254
12. C.S. Prajapati, A. Kushwaha, and P.P. Sahay, Experimental Investigation of Spray-Deposited Fe-Doped ZnO Nanoparticle Thin Films: Structural, Microstructural, and Optical Properties, *J. Therm. Spray Technol.*, 2013, **22**(7), p 1230–1241
13. F.L. Toma, G. Bertrand, S. Begin, C. Meunier, O. Barres, D. Klein, and C. Coddet, Microstructure and Environmental Functionalities of TiO_2-Supported Photocatalysts Obtained by Suspension Plasma Spraying, *Appl. Catal. B Environ.*, 2006, **68**(1–2), p 74–84
14. Z. Hamden, S. Boufi, D.S. Conceicao, A.M. Ferraria, A.M. Botelho do Rego, D.P. Ferreira, L.F. Vieira Ferreira, and S. Bouattour, Li-N Doped and Codoped TiO_2 Thin Films Deposited by Dip-Coating: Characterization and Photocatalytic Activity under Halogen Lamp, *Appl. Surf. Sci.*, 2014, **314**, p 910–918
15. R. Saravanan, S. Karthikeyan, V.K. Gupta, G. Sekaran, V. Narayanan, and A. Stephen, Enhanced Photocatalytic Activity of ZnO/CuO Nanocomposite for the Degradation of Textile Dye on Visible Light Illumination, *Mater. Sci. Eng. C Mater.*, 2013, **33**, p 91–98
16. N. Chandrasekharan and P.V. Kamat, Improving the Photoelectrochemical Performance of Nanostructured TiO_2 Films by Adsorption of Gold Nanoparticles, *J. Phys. Chem.*, 2000, **104**(46), p 10851–10857
17. L.J. Guo, J.W. Luo, T. He, S.H. Wei, and S.S. Li, Photocorrosion-Limited Maximum Efficiency of Solar Photoelectrochemical Water Splitting, *Phys. Rev. Appl.*, 2018, **10**(6), p 064059
18. H. Wang, L. Zhang, Z. Chen, J. Hu, S. Li, Z. Wang, J. Liu, and X. Wang, Semiconductor Heterojunction Photocatalysts: Design, Construction, and Photocatalytic Performances, *Chem. Soc. Rev.*, 2014, **43**(15), p 5234–5244
19. D.R. Baker and P.V. Kamat, Photosensitization of TiO_2 Nanostructures with CdS Quantum Dots: Particulate Versus Tubular Support Architectures, *Adv. Funct. Mater.*, 2009, **19**(5), p 805–811
20. J. Zhang, J.-H. Bang, C. Tang, and P.V. Kamat, Tailored TiO_2-$SrTiO_3$ Heterostructure Nanotube Arrays for Improved Photoelectrochemical Performance, *ACS Nano*, 2010, **4**(1), p 387–395
21. H. Kato and A. Kudo, Visible-Light-Response and Photocatalytic Activities of TiO_2 and $SrTiO_3$ Photocatalysts Codoped with Antimony and Chromium, *J. Phys. Chem.*, 2002, **106**(19), p 5029–5034
22. F. Davar, M. Salavati-Niasari, and S. Baskoutas, Temperature Controlled Synthesis of $SrCO_3$ Nanorods via a Facile Solid-State Decomposition Rout Starting from a Novel Inorganic Precursor, *Appl. Surf. Sci.*, 2011, **257**(9), p 3872–3877
23. N. Tipcompor, T. Thongtem, A. Phuruangrat, and S. Thongtem, Characterization of $SrCO_3$ and $BaCO_3$ Nanoparticles Synthesized by Cyclic Microwave Radiation, *Mater. Lett.*, 2012, **87**, p 153–156
24. J. Fu, G.Z. Kyzas, Z.Q. Cai, E.A. Deliyanni, W. Liu, and D.Y. Zhao, Photocatalytic Degradation of Phenanthrene by Graphite Oxide-TiO_2-$Sr(OH)_2$/$SrCO_3$ Nanocomposite Under Solar Irradiation: Effects of Water Quality Parameters and Predictive Modeling, *Chem. Eng. J.*, 2018, **335**, p 290–300
25. S. Jin, G.H. Dong, J.M. Luo, F.Y. Ma, and C.Y. Wang, Improved Photocatalytic NO Removal Activity of $SrTiO_3$ by Using $SrCO_3$ as a New Co-catalyst, *Appl. Catal. B Environ.*, 2018, **227**, p 24–34
26. F.L. Toma, L.M. Berger, T. Naumann, and S. Langner, Microstructures of Nanostructured Ceramic Coatings Obtained by Suspension Thermal Spraying, *Surf. Coat. Technol.*, 2008, **202**(18), p 4343–4348
27. L. Pawlowski, Suspension and Solution Thermal Spray Coatings, *Surf. Coat. Technol.*, 2009, **203**(19), p 2807–2829
28. X. He, Y. Liu, J. Huang, X. Chen, K. Ren, and H. Li, Adsorption of Alginate and Albumin on Aluminum Coatings Inhibits Adhesion of Escherichia Coli and Enhances the Anti-corrosion Performances of the Coatings, *Appl. Surf. Sci.*, 2015, **332**, p 89–96
29. P. Fauchais and G. Montavon, Latest Developments in Suspension and Liquid Precursor Thermal Spraying, *J. Therm. Spray Technol.*, 2010, **9**(1–2), p 226–239

30. T.T. Parlak, F. Apaydin, and K. Yildiz, Formation of $SrTiO_3$ in Mechanically Activated $SrCO_3$-TiO_2 System, *J. Therm. Anal. Calorim.*, 2017, **127**(1), p 63–69
31. A. Fujishima, X.T. Zhang, and D.A. Tryk, TiO_2 Photocatalysis and Related Surface Phenomena, *Surf. Sci. Rep.*, 2008, **63**(12), p 515–582
32. X. Zhang, N. Sun, B. Wu, Y. Lu, T. Guan, and W. Wu, Physical Characterization of Lansoprazole/PVP Solid Dispersion Prepared by Fluid-Bed Coating Technique, *Powder Technol.*, 2008, **182**(3), p 480–485
33. Z.H. Du, T.S. Zhang, M.M. Zhu, and J. Ma, PVP-Mediated Crystallization of Perovskite Phase in the PMN-PT Thin Films Prepared by Sol-Gel Processing, *J. Am. Ceram. Soc.*, 2013, **93**(3), p 686–691
34. H. Kozuka and S. Takenaka, Single-Step Deposition of Gel-Derived Lead Zirconate Titanate Films: Critical Thickness and Gel Film to Ceramic Film Conversion, *J. Am. Ceram. Soc.*, 2002, **85**(11), p 2696–2702
35. J.R. de Oliveira Lima, Y.A. Ghani, R.B. da Silva, F.M.C. Batista, R.A. Bini, L.C. Varanda, and J.E. de Oliveira, Strontium Zirconate Heterogeneous Catalyst for Biodiesel Production: Synthesis, Characterization and Catalytic Activity Evaluation, *Appl. Catal. A Gen.*, 2012, **445**, p 76–82
36. C. Belver, R. Bellod, A. Fuerte, and M. Fernandez-Garcia, Nitrogen-Containing TiO_2 Photocatalysts—Part 1. Synthesis and Solid Characterization, *Appl. Catal. B Environ.*, 2006, **65**(3–4), p 301–308
37. O. Wiranwetchayan, S. Promnopas, T. Thongtem, A. Chaipanich, and S. Thongtem, Effect of Alcohol Solvents on TiO_2 Films Prepared by Sol-Gel Method, *Surf. Coat. Technol.*, 2017, **326**, p 310–315
38. S.F. Yang, C.G. Niu, D.W. Huang, H. Zhang, C. Lianga, and G.-M. Zeng, $SrTiO_3$ Nanocubes Decorated with Ag/AgCl Nanoparticles as Photocatalysts with Enhanced Visible-Light Photocatalytic Activity Towards the Degradation of Dyes, Phenol and Bisphenol A, *Environ. Sci Nano*, 2017, **4**(3), p 585–595
39. M.S. Falcao, M.A.S. Garcia, C.V.R. de Moura, S. Nicolodi, and E.M. de Moura, Synthesis, Characterization and Catalytic Evaluation of Magnetically Recoverable SrO/$CoFe_2O_4$ Nanocatalyst for Biodiesel Production from Babassu Oil Transesterification, *J. Brazil. Chem. Soc.*, 2018, **29**(4), p 845–855
40. R. Gonzalez, H. Ashrafizadeh, A. Lopera, P. Mertiny, and A. McDonald, A Review of Thermal Spray Metallization of Polymer-Based Structures, *J. Therm. Spray Technol.*, 2016, **25**(5), p 897–919
41. D.A.H. Hanaor and C.C. Sorrell, Review of the Anatase to Rutile Phase Transformation, *J. Mater. Sci.*, 2011, **46**(4), p 855–874
42. C. Luo, J. Zhao, Y. Li, W. Zhao, Y. Zeng, and C. Wang, Photocatalytic CO_2 Reduction Over $SrTiO_3$: Correlation Between Surface Structure and Activity, *Appl. Surf. Sci.*, 2018, **447**, p 627–635
43. R.L. Penn and J.F. Banfield, Imperfect Oriented Attachment: Dislocation Generation in Defect-Free Nanocrystals, *Science*, 1998, **281**(5379), p 969–971
44. X. Chen, L. Liu, P.Y. Yu, and S.S. Mao, Increasing Solar Absorption for Photocatalysis with Black Hydrogenated Titanium Dioxide Nanocrystals, *Science*, 2011, **331**(6018), p 746–750
45. U. Diebold, The Surface Science of Titanium Dioxide, *Surf. Sci. Rep.*, 2003, **48**(5–8), p 53–229
46. M. Ahmad, E. Ahmed, Z.-L. Hong, J.F. Xu, N.R. Khalid, A. Elhissi, and W. Ahmed, A Facile One-Step Approach to Synthesizing ZnO/Graphene Composites for Enhanced Degradation of Methylene Blue Under Visible Light, *Appl. Surf. Sci.*, 2013, **274**, p 273–281
47. D. Reyes-Coronado, G. Rodríguez-Gattorno, M.E. Espinosa-Pesqueira, C. Cab, R. de Coss, and G. Oskam, Phase-Pure TiO_2 Nanoparticles: Anatase, *Brookite and Rutile. Nanotechnology*, 2008, **14**(9), p 145605
48. M. Tata, S. Banerjee, V.T. John, Y. Waguespack, and G.L. McPherson, Fluorescence Quenching of CdS Nanocrystallites in AOT Water-in-oil Microemulsions, *Colloids Surf. A*, 1997, **127**(1–3), p 39–46
49. T. Saito, T. Iwase, J. Horie, and T. Morioka, Mode of Photocatalytic Bactericidal Action of Powdered Semiconductor TiO_2 on Mutans Streptococci, *J. Photochem. Photobiol. B*, 1992, **14**(4), p 369–379